



# Influence and comparison of contaminate partitioning on nanocrystalline stability in sputter-deposited and ball-milled Cu–Zr alloys

Xuyang Zhou<sup>1</sup>, Jennifer D. Schuler<sup>2</sup>, Charlette M. Grigorian<sup>2</sup>, David Tweddle<sup>1</sup>, Timothy J. Rupert<sup>2</sup>, Lin Li<sup>1</sup>, and Gregory B. Thompson<sup>1,\*</sup>

<sup>1</sup>Department of Metallurgical and Materials Engineering, The University of Alabama, Tuscaloosa, AL, USA

<sup>2</sup>Department of Materials Science and Engineering, University of California, Irvine, Irvine, CA, USA

Received: 19 July 2020

Accepted: 22 July 2020

Published online:  
10 September 2020

© Springer Science+Business  
Media, LLC, part of Springer  
Nature 2020

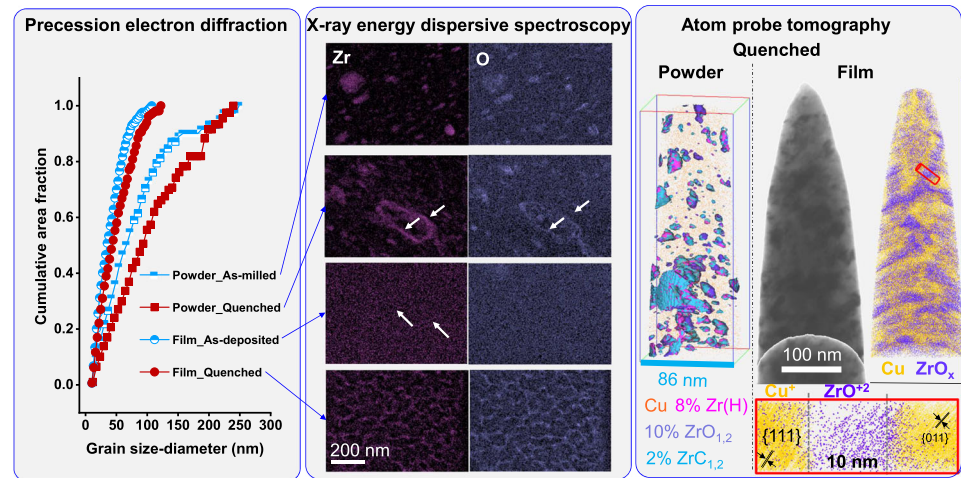
## ABSTRACT

Ascertaining the mechanism(s) of nanocrystalline stability is a critical need in revealing how specific alloys retard grain growth. Often significant debate exists concerning such mechanisms, even in the same alloy. Here, we compare two processing methods—high-energy ball milling and thin film deposition—in the fabrication and subsequent two-step annealing (500 °C/24 h followed by a temperature ramp to 900 °C whereupon the sample was held for 1 min and quenched) for nanocrystalline Cu–Zr. Using precession electron diffraction (PED) and atom probe tomography (APT), the grain stability and secondary phase content was quantified. The milled powder sample revealed that the Zr solute was largely in an oxide/carbide state after milling with no significant change upon annealing. In contrast, the thin film sample showed nearly all elemental Zr upon deposition but significant oxidation after the vacuum anneal. The significant uptake of oxygen is contributed to the high surface area-to-volume ratio of the film coupled with columnar grains that were enriched in elemental Zr in the as-deposited state. Furthermore, upon sputter deposition, many of these boundaries were vitrified which was lost upon annealing. These glassy boundaries were not observed by PED of the powders. The consequence of when the solute reacts with contaminate species is discussed in relation to nanocrystalline and microstructural stability. The use of Zener pinning predicted grain sizes, based on the quantification of the secondary phase particulates measured by APT, are given to better ascertain their contribution to nanocrystalline stability.

Handling Editor: Nathan Mara.

Address correspondence to E-mail: gthompson@eng.ua.edu

## GRAPHIC ABSTRACT



## Introduction

With the reduction of grain size, significant improvements in a material's mechanical properties, such as hardness, strength, and wear resistance, are known to occur [1–7]. However, a smaller grain size results in an increase in thermodynamic instability, which scales as the inverse of the radius of curvature of the grain [8–10]. Considerable interest has developed in stabilizing these small grains from coarsening in order to retain their superior properties. The primary mechanisms of stabilization are essentially either thermodynamic and/or kinetic. The thermodynamic approach is achieved through chemical alloying, in which the solutes segregate and decorate the grain boundary [7, 11–18]. These solutes decrease the grain boundary energy resulting in a reduction of the driving force for grain growth [11, 12, 19, 20]. Alternatively, in the kinetic design, solute clusters provide a Zener pinning and/or drag effect, which act to reduce grain boundary mobility [7, 13, 21–23]. Recent studies have even suggested that when solute atoms are present at particular boundaries, the local equilibrium structure can be tailored, termed “complexion engineering” [24, 25]. This too can alter the boundary's physical properties and growth behavior.

The nanocrystalline stabilized alloy Cu–Ta has received considerable attention because of its clear

stability up to homologous temperatures near  $0.9 T_M$  (melting point) [26, 27]. This grain boundary stability has been linked to the increased energy barrier for grain boundary sliding and rotation resulting in remarkable creep resistance [7]. This is especially peculiar considering that small grain materials are notorious for poor creep resistance. Similar to other Cu-based nanocrystalline alloys, such as Cu–W [17] and Cu–Nb [28], the Cu–Zr alloy, they too have been reported as a nanocrystalline stabilized system [29–33]. Unlike the other two Cu-solute alloys, in which a miscibility gap is present, the Cu–Zr system can form several intermetallic phases providing a potentially different stabilization behavior. At high solute concentrations, this alloy can even vitrify upon sputter deposition [34]. At high Zr concentrations within Cu(Zr) alloy grain boundaries, they can cause the boundaries to vitrify, termed as an amorphous intergranular film (AIF) by Schuler et al. [32]. Khalajhedayati et al. [31] suggested that these AIFs could even result in a unique combination of strength and ductility for stabilized nanocrystalline alloys. Even at very small Zr concentrations, the Zr solute has a potent effect on microstructure stability. Atwater et al. [29] reported that a Cu-1 at% Zr retained nanoscale grain sizes up to  $0.85 T_M$ , while Khalajhedayati and Rupert [30] reported retarded grain

growth after a week of annealing at 98% the solidus temperature for a Cu-3 at% Zr alloy.

Unfortunately, the exact stabilization mechanism can be convoluted by solute interactions with the annealing atmosphere, creating secondary phases. For example, the stabilization of nanostructured Fe-Mg has been attributed to both solute interaction and nanoscale oxidation from Fe's and Mg's high affinity for O [18]. Similarly, Kapoor et al. [28] revealed the formation of oxide, nitride, and carbide clusters at grain boundaries in nanostructured, ball-milled Cu-Nb. Marvel et al. [35] even described nanoscale oxides of sufficient size and volume fraction in nanocrystalline Ni-W alloys to inhibit grain growth by a particle drag mechanism. In later work, Marvel et al. [36] reported the formation of a contaminant carbide  $\text{Ni}_6\text{W}_6\text{C}$  in electroplated nanocrystalline Ni-23 at% W alloys annealed at 700 °C that could provide a similar stabilizing effect on the grain size. Since W in Ni has a low enthalpy of segregation to the grain boundaries, the influence of these types of impurity phases forming at grain boundaries has a profound effect on correctly identifying the stabilization mechanism.

With regards to the Cu-Zr system, Zr readily forms carbides and oxides because of its highly negative formation enthalpies of  $-207$  kJ/mol [37] and  $-1097$  kJ/mol [38], respectively. In this system, contamination is almost inevitable, even when attempting to anneal the material in a vacuum or in an Ar atmosphere. Though these phases have been reported at grain boundaries in this material, the dominant stabilization method specified in the literature is thermodynamic stabilization, i.e., the reduction of grain boundary energy or the AIF [30]. This may be in part because of the difficulty in assessing the presence of these impurities and associated reaction products. The inability for impurity phase detection could be ascribed to low volume fraction (limiting diffraction evidence), the size of such phases (i.e., the ability to observe them), and the chemical detection of the species by X-ray Energy Dispersive Spectroscopy (XEDS), which has a lower efficiency and accuracy for low atomic number elements like C and O. Nevertheless, one method that can provide equal sensitivity for all elements, in addition to high chemical and spatial resolution, is atom probe tomography (APT) [39]. To the authors' knowledge, there are only a few papers that have applied APT to characterize nanocrystalline Cu-Zr alloys, with most

focused on structural applications concerning crystalline-amorphous nanolaminates and not necessarily on the impurity content, its distribution, or effects [33, 40–42].

In this work, we will employ APT to quantify the contamination and spatial distribution of the Zr solute at Cu-Zr grain boundaries produced by two means—high-energy ball milling and sputter deposition. Ball milling is generally considered a processing method more susceptible to contamination because of container and milling media impurity pick-up upon powder deformation. In contrast, thin film deposition is considered 'cleaner' as it is done in an (ultra) high vacuum deposition condition with direct nanocrystalline formation. Both methods are commonly used in nanocrystalline synthesis studies, where intrinsic contamination contributions to their nanocrystalline stability are largely absent in the discussion of the findings or underreported. The lack of detailed (or appropriate scale) characterization can then inadvertently promote stabilization mechanism ideas that are not accurate. Such outcomes adversely affect theory development with the associated fundamental science that underpins the means to engineer nanocrystalline alloys. Thus, the distinct contribution of this work is assessing the processing method effect in studying nanocrystalline stability with the appropriate characterization methods that reveal such mechanisms.

## Experimental

The ball-milled alloy was prepared by mixing elemental powders to a target Cu-3 at% Zr composition. Subsequent characterization of the specific powder studied showed a lower Zr concentration ( $\sim 1$  at%) than expected, possibly due to compositional variations from particle-to-particle. We therefore report the experimentally determined composition of the ball-milled sample as Cu-1Zr to be consistent to what was characterized. The mixed powders were placed into a hardened steel vial with hardened steel milling media under an Ar gas environment and milled for 10 h. Stearic acid (1 wt%) was added to the mixture to prevent cold welding. Post-milling, a subset of powders was set aside and will be referred to as the 'as-milled condition.' The remaining powder particles, which were  $\sim 10$   $\mu\text{m}$  in size, was annealed under vacuum at 500 °C for 24 h followed by

temperature ramp to 900 °C for 1 min with a concluding water quench via a custom drop vacuum tube. The rationale for the two-step annealing can be found in Ref. [32]. These samples will be referred to as the heat-treated or annealed powders.

The thin film samples were co-sputter deposited from elemental targets of 99.99 wt% for Cu and 99.2 wt% (inc. Hf, an intrinsic contaminate) for Zr. The film was grown to an approximate thickness of 2  $\mu\text{m}$  onto the surface of two polished  $\sim 13 \text{ mm} \times \sim 12 \text{ mm} \times \sim 1 \text{ mm}$  thick Cu substrates. The base vacuum pressure prior to deposition was  $< 1.3 \times 10^{-5} \text{ Pa}$  whereupon ultra-high purity argon was flowed into the chamber to a pressure of 0.2 Pa and served as the working gas for the plasma. After deposition, one substrate was set aside and will be referred to as the as-deposited film. The other film was encapsulated under vacuum, annealed, and quenched using the same procedure described previously and will be referred to as the heat-treated or annealed film. Chemical characterization of the film revealed the composition to be Cu–3Zr, as termed henceforth.

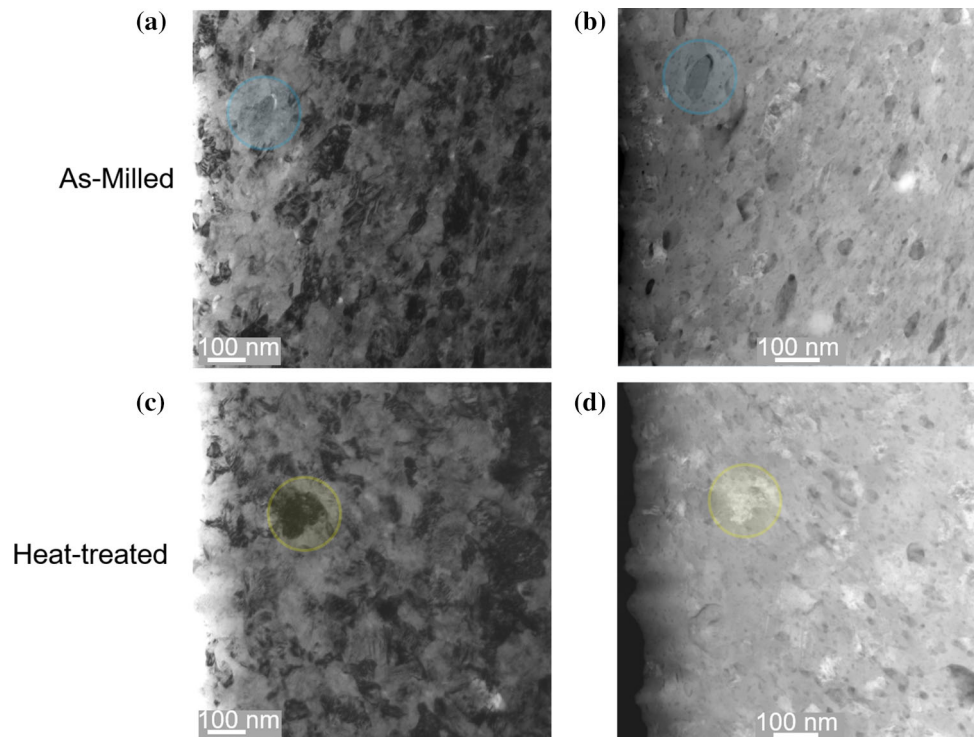
Phase, microstructure, and chemical distribution of each sample were determined using an FEI Tecnai F20 Scanning TEM ((S) TEM) operated at 200 keV. The TEM samples were prepared by traditional focused ion beam (FIB) methods using a FEI Quanta 3D dual-beam FIB-Scanning Electron Microscope (SEM). The powder samples were initially embedded in an epoxy resin at room temperature under atmospheric pressure and allowed to cure for 24 h. The powders, now in a mounted fixture, were then metallographically polished to a mirror surface finish. For the thin film sample, the TEM wedge was directly FIB lifted-out from the deposited surface, similar to prior preparation reports [43] revealing the cross section of the deposited film. In addition, a plan-view TEM foil was prepared where the foil was FIB extracted and milled by rotating the film 90° to the deposition direction and extracting the foil [43]. The grain morphology in both viewing directions was imaged in bright field (BF) as well as with atomic number,  $Z$ , contrast using a high angle annular dark-field (HAADF) detector. When taking the HAADF images, the camera length was set to 100 mm to mitigate the contribution of Bragg diffraction to the contrast. Grain sizes and orientation distributions were quantified by using the precession electron diffraction (PED) technique on the NanoMegas

ASTAR™ platform [44–46]. The PED scans were taken at a 0.3° precession angle at a scanning step size of 3 nm over a 2.0  $\mu\text{m} \times 0.9 \mu\text{m}$  region of interest (ROI). After scanning, the data was converted for analysis using the TSL OIM Analysis 7 software package. Grain-based misorientation analyses have been employed to identify the grains with varying local misorientations. XEDS mapping was also collected to compare to the APT results using an EDAX® silicon drift detector (SDD).

APT analysis was performed using a Cameca® Instruments Local Electrode Atom Probe (LEAP) 5000 XS with a detection efficiency of  $\sim 80\%$ . Similarly to TEM foils, a FIB lift-out technique [43, 47] was employed to prepare the APT tips into the required needle-like tip needed for field evaporation using the aforementioned FEI Quanta 3D dual-beam FIB-SEM or Tescan Lyra dual-beam FIB. A 5 keV clean-up step was applied at the end of each milling step to reduce Ga<sup>+</sup> implanted surface damage. Once sharpened, the tips were field evaporated at a specimen temperature of 40 K, laser pulse energy of 100 pJ with a pulse repetition rate of 625 kHz for a 0.8% atoms per pulse detection rate. The APT data was reconstructed using the IVAS 3.8.2 software platform. As many of the forthcoming datasets used isoconcentration surfaces to study the chemical partitioning, the selection of both the isoconcentration element and the value used to create the surface was dependent on the extent of partitioning. We followed references [48, 49] in our selection of the appropriate isoconcentration values for this analysis.

A correlative TEM-PED and APT approach was also conducted. Though APT provides high spatial chemical mapping, it does not collect all of the atoms nor has perfect lattice rectification. Consequently, TEM diffraction can be used to identify the grain boundaries unambiguously as well as their character via PED. Cross-correlating the two sets of images provides a complete chemical and structural quantification of the grain boundaries within the APT tip. Thus, prior to field evaporation, a series of APT tips were mounted to a Si half grid holder rather than the normally used coupon [43, 50]. This enabled the grid to go between the TEM, mounted in a specially designed Hummingbird TEM-APT holder, and the LEAP. The grain-to-grain mapping of the APT was done using PED, but now at a step size of 2 nm and a precession angle of 0.3°. A chemical spatial map, via XEDS, was also performed on each tip as a

**Figure 1** a BF and b HAADF image of the as-milled Cu–1Zr sample. c BF and d HAADF images of the heat-treated Cu–1Zr sample. The circled regions provide a guide to the eye in correlating features between the two sets of images.



comparison to the APT mapping. Further detailed PED and APT cross-correlative information can be found in [43].

## Results

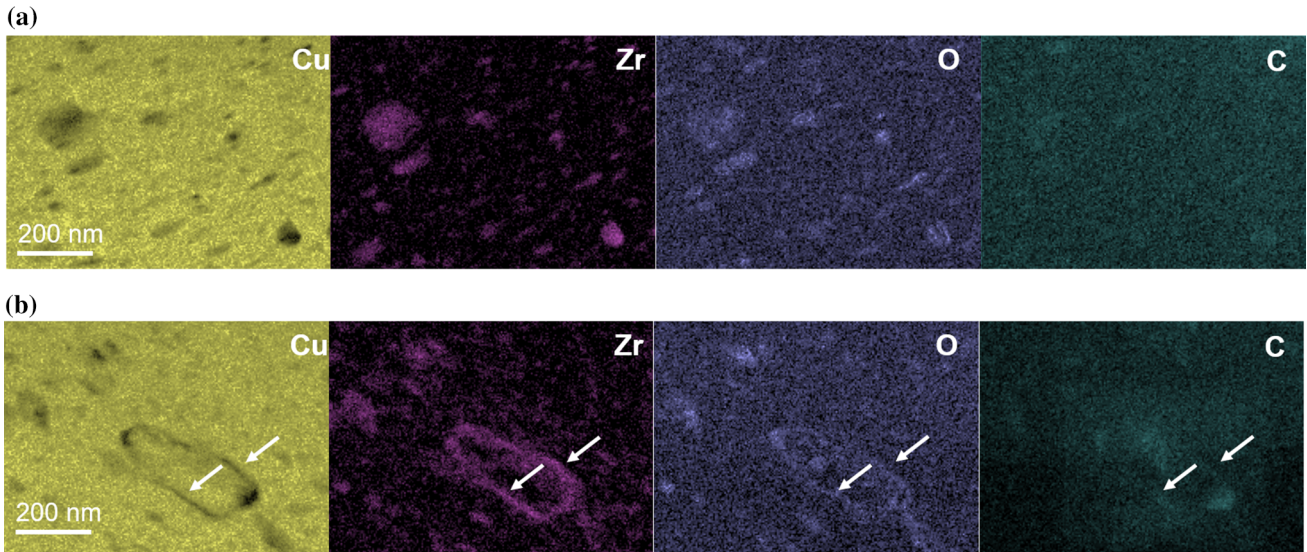
### Bulk milling

Figure 1a, b show the BF and STEM-HAADF images of the as-milled powder of the Cu–1Zr (at%) sample. The multiple bright contrast granular features in the BF image indicates a nanocrystalline grain structure. Spherical precipitates, with bright and dark contrast, observed within the HAADF image of this nanostructure indicating different phases dependent upon chemical composition. As a comparison, the nanostructure after the heat treatment is shown in the BF image, Fig. 1c, and the HAADF image, Fig. 1d, where no major microstructure variations can be observed between the as-milled and annealed samples.

In Fig. 2, XEDS mapping was used to ascertain an overview of the chemical distribution of the Zr solute, with the overall Zr composition being measured as  $\sim 1$  at% for the powder samples. The chemical mapping of contaminants, i.e., O and C, were also included. As shown in Fig. 2a, b's spectral images, the Zr was phase-separated from the Cu

matrix with the Zr-rich regions being relatively spherical or oval in morphology. Both small clusters, with sizes near  $\sim 10$  nm, and large clusters,  $\sim 100$  nm (and even larger) were detected. This suggests inhomogeneity in the Zr distribution in the ball milling process, which could be suspected by the targeted composition and studied powder compositions being different. Some of these Zr clusters appear to align themselves along the grain boundaries. The white arrows in Fig. 2b help direct the reader's attention to specific Zr partitioning outlining multiple grains; a clear indication of grain boundary segregation. Khalajhedayati et al. [31] reported that such segregation can favor the formation of AIFs. In this work, we intend to further explore the chemistry of those Zr segregated grain boundary regions developed later in the article. O and C detected signals were also found in the spectral map. It is relatively easy to distinguish the O-rich region, since they tracked well with Zr segregated regions. In contrast, the C spectral map was found to be rather uniform in the as-milled condition with more apparent partitioning following annealing.

APT was employed to capture and quantify the finer scale chemical partitioning in these two samples. Figure 3 is the mass spectra of the as-milled and heat-treated states with similar peaks detected in



**Figure 2** XEDS elemental Cu, Zr, O, C maps of the **a** as-milled and **b** heat-treated Cu-1Zr sample.

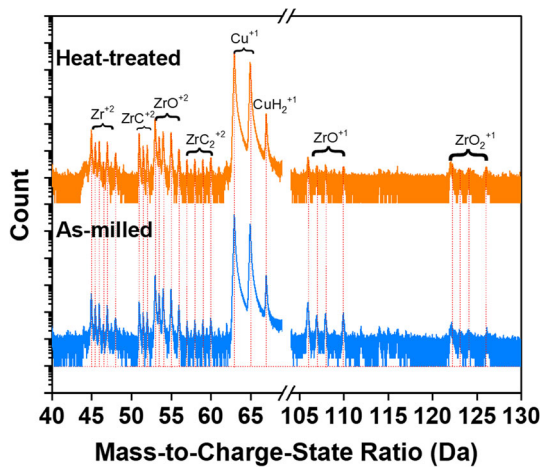


**Figure 3** Atom probe mass spectra of the as-milled and heat-treated Cu-1Zr samples.

both specimens. The overall bulk composition is shown in Table 1. Note that copper hydride was included in the total elemental copper count. In the mass spectrums, the various complexes of Zr’s field evaporation are noted by  $ZrC^{+2}$ ,  $ZrO^{+2}$ ,  $ZrC_2^{+2}$ ,

$ZrO^{+1}$ , and  $ZrO_2^{+1}$  states. The APT results indicate the presence of O- and C-rich Zr particles, with more than half of the detected Zr atoms coupled in a complex state with either C or O. Since these C- and O-rich Zr particles were detected in the as-milled sample, the contamination source is likely contributed to the stearic acid needed during the milling process to prevent cold welding [30]. Furthermore, the presence of copper hydride could also be a result of stearic acid contamination, though the detection of ambient hydrogen is commonly reported in the analysis chamber during field evaporation [51].

Figure 4 displays the atom maps for the as-milled Cu-1Zr sample. The isoconcentration surfaces from the different evaporation states of Zr, i.e.,  $Zr(H)$ ,  $ZrO_{1,2}$ ,  $ZrC_{1,2}$ , are shown overlaid on top of the Cu atom map (Fig. 4a). The subscripts of 1, 2 refer to the number of C or O present in the molecular ion detected. These contaminate species were largely identified through their complex ion states. A large cluster, as marked by a red arrow, and small clusters, highlighted by black arrows, are noted within this

**Table 1** Elemental compositions as measured by APT

| Element at% | Powder       |              | Film         |              |
|-------------|--------------|--------------|--------------|--------------|
|             | As-milled    | Heat treated | As-deposited | Heat treated |
| Cu          | 97.5 ± 0.015 | 97.4 ± 0.016 | 96.0 ± 0.019 | 91.4 ± 0.018 |
| Zr          | 1.0 ± 0.001  | 1.1 ± 0.001  | 3.8 ± 0.003  | 2.5 ± 0.002  |
| O           | 0.8 ± 0.001  | 0.7 ± 0.001  | 0.2 ± 0.001  | 5.1 ± 0.003  |
| C           | 0.3 ± 0.001  | 0.5 ± 0.001  | 0.0 ± 0.000  | 0.6 ± 0.001  |
| N           | 0.3 ± 0.001  | 0.4 ± 0.001  | 0.1 ± 0.000  | 0.4 ± 0.001  |

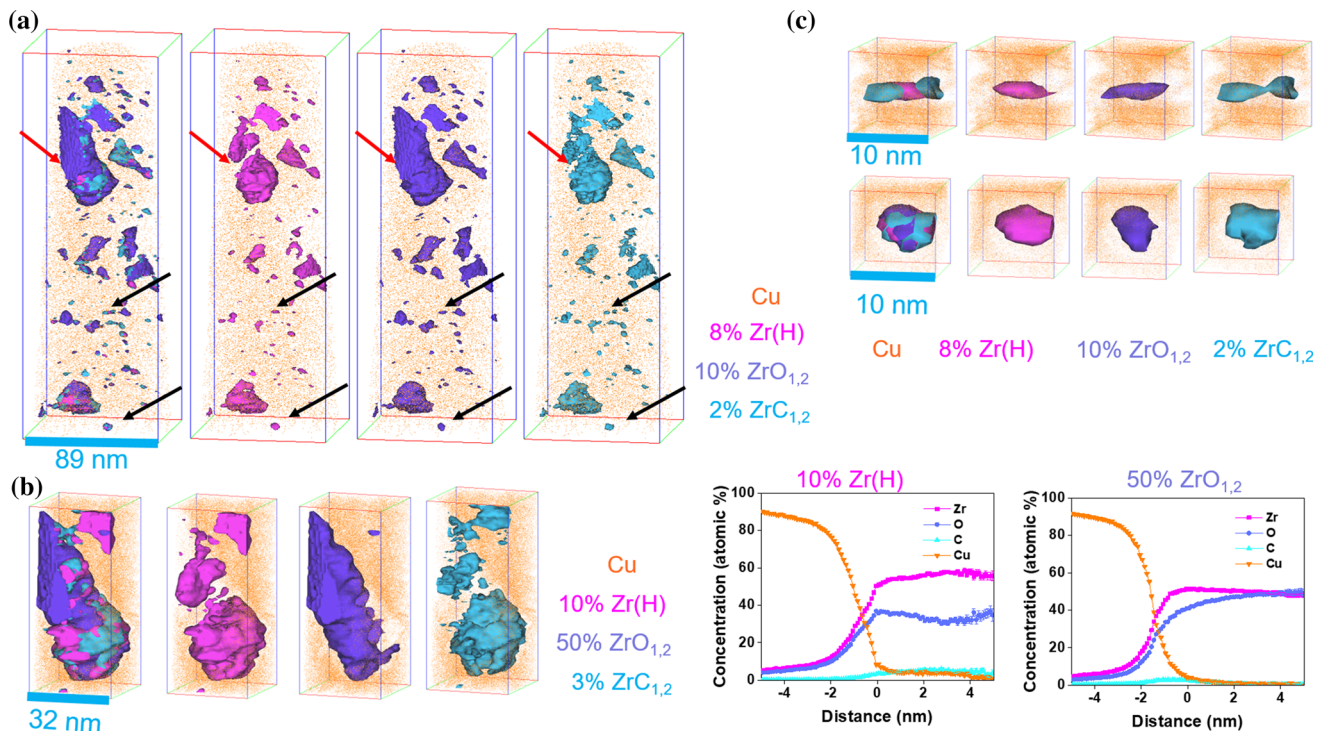


**Figure 4** **a** Atom maps of the as-milled Cu–Zr samples. **b** Atom maps of a large second phase and the corresponding proxigram from the 10 ionic% Zr(H) isoconcentration surface and the 50 ionic% ZrO<sub>1,2</sub> isoconcentration surface. **c** Atom maps of small

APT dataset. These features are consistent with the previous XEDS spectral map that showed various sized secondary phases, Fig. 2. As displayed in the enlarged image for a single large particle, Fig. 4b, elemental Zr ions and ZrC<sub>1,2</sub> ions occupy the bottom portion of the particle while the ZrO<sub>1,2</sub> ions reside in the upper part of the particle. The proxigram in Fig. 4b reveals the chemical partitioning within this particle.

In the upper row of images in Fig. 4c, a flattened precipitate with a carbon-rich region (identified by the ZrC<sub>1,2</sub> complexes) on the outer surface and the presence of elemental Zr and oxygen (identified by Zr ions and ZrO<sub>1,2</sub> complexes) in the core region are displayed. This suggests a sequential reaction as the solute came into contact with the different impurities. Though this particular particle is chemically asymmetric, this is not the case for all particles analyzed. For example, in Fig. 4c—the lower series of images—a smaller particle occupied by Zr, O, and C appears to have a uniform chemical distribution throughout.

This distribution of different sizes and compositions for the particles was also observed in the heat-treated Cu–Zr sample, Fig. 5a. Figure 5b shows

particles. The top line images show clusters with uniform ion distribution and the bottom line images show those with non-uniform ion distribution.

Zr(H) and ZrC<sub>1,2</sub> appearing to co-segregate, while ZrO<sub>1,2</sub> ions are located in different regions around the secondary phase, with these differences highlighted with black circles in Fig. 5b. The corresponding proxigrams from the isoconcentration surfaces are shown in Fig. 5b. Similar to the as-milled sample, we observed both non-uniform and uniform chemical distributions of carbon and oxygen in the smaller Zr-rich particles (Fig. 5c). From the APT data, we can conclude that the majority of Zr is found in Zr-rich or O-rich particles with much lower concentrations of C found in these regions.

PED orientation maps of the as-milled and heat-treated powder samples are shown in Fig. 6a, b. The PED scans reveal well-defined grain boundaries that are not equiaxed but elongated in specific directions. This anisotropic granular morphology is a result of the deformation from the ball milling process. It also indicates that some particles were not well milled. The PED scans also reveal a mosaic of colors that represent multiple grain orientations, which is further confirmed by the three different pole figures placed at the bottom of those images. The majority of the scanned region has been identified as

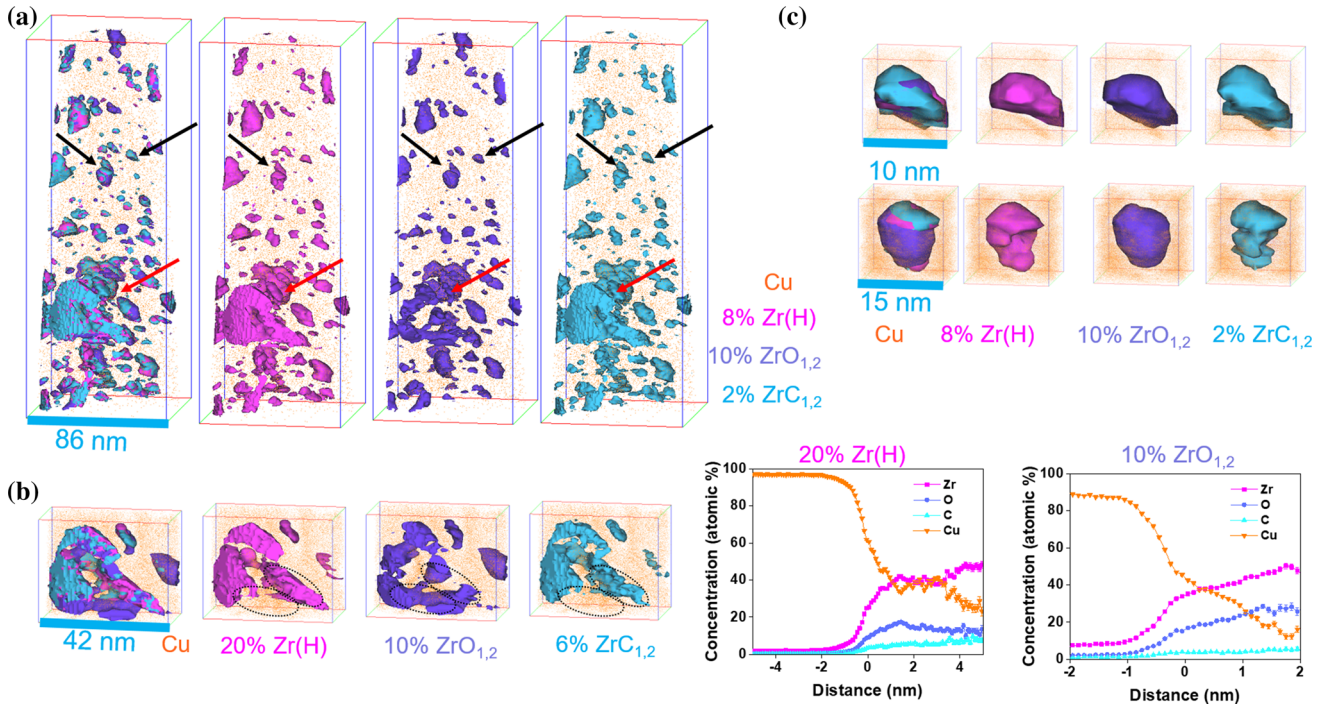


**Figure 5** **a** Atom maps of the heat-treated Cu–Zr samples. **b** Atom maps of a large second phase and the corresponding proxigrams from the 20 ionic % Zr(H) isoconcentration surface and the 10 ionic % ZrO<sub>1,2</sub> isoconcentration surface. **c** Atom maps

of smaller clusters. The top line images show particles with uniform ion distribution and the bottom line images show those with non-uniform ion distribution.

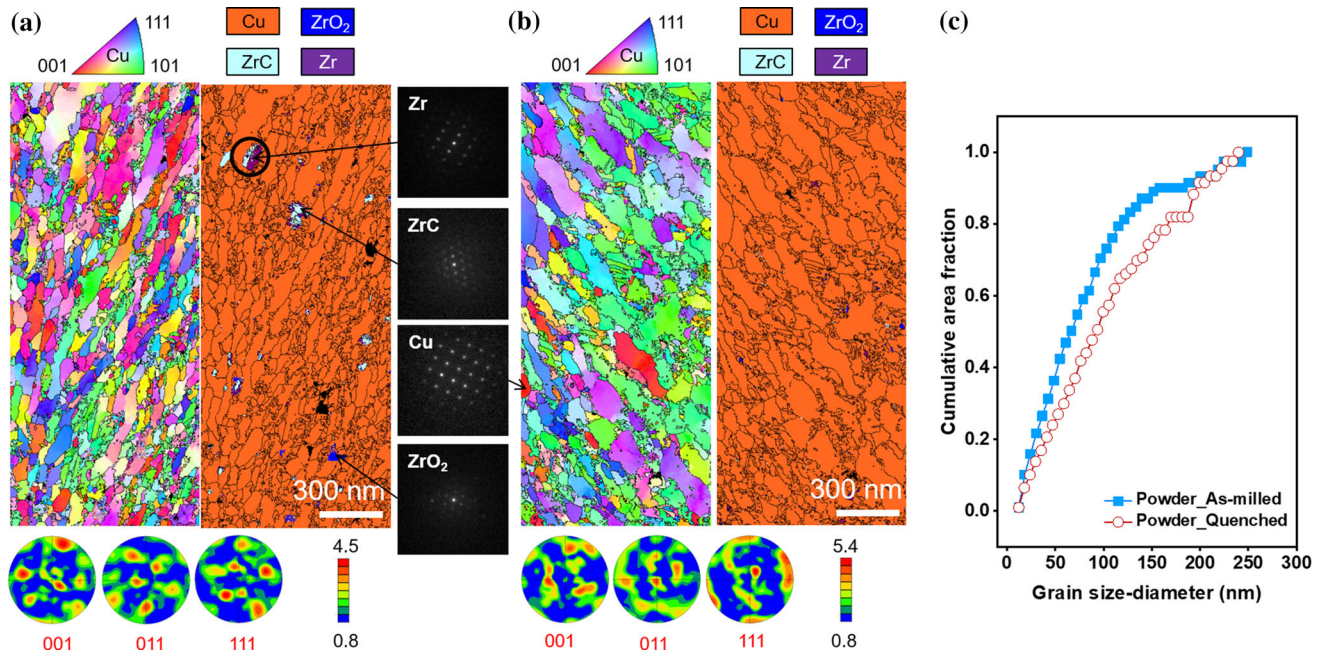


**Figure 6** PED orientation maps, phase map, pole figures, and selected diffraction patterns of the **a** as-milled and **b** heat-treated Cu–Zr samples. **c** Cumulative grain size plots from (a) &(b).

Note the circled region in (a) revealing the presence of Zr and ZrC in contact with each other, revealing how contaminant reactions consumed the elemental solute phase.

face-centered cubic Cu along with some minor phases identified as Zr (ICSD 52544), ZrO<sub>2</sub> (ICSD 56696), and ZrC (ICSD 22264) in both the as-milled and heat-treated states. Besides the preferred ZrO<sub>2</sub> phase, ZrO (ICSD 76019) could also exist because of an O-lean environment and the ability to co-segregate with ZrC. Both the mono-oxide and mono-carbide phases have the rock-salt crystal structure with a similar lattice parameter, 0.4669 nm for ZrC and 0.4602 nm for ZrO. The close proximity of both contaminant species in the APT results further supports the likelihood that some of the secondary phases are a mixed carbo-oxide. Finally, no amorphous diffraction patterns were captured by the PED scan, with such regions being associated with the aforementioned AIF discussed in the introduction. However, since the resolution of PED is  $> \sim 3$  nm and AIFs are reported to be at or smaller than this size [31], it is not possible to exclude their presence in these particular scans.

The PED area fraction for all of the precipitates, including, Zr, ZrO<sub>2</sub>, and ZrC, was 2.6% in the as-milled condition, while after annealing these phases accounted for 0.7%. Normally, high temperature exposure facilitates further phase separation and more potential chemical reactions, but it is also possible that some of the impurity phases decrease with annealing [52]. This phase fraction variance is attributed to the aforementioned issues of ball milling's inability to achieve micro-homogeneity for the solute distributions. Cumulative grain size distributions for both of these processed states is given in Fig. 6c. After the heat treatment, the grain size slightly increased from the average value of  $76 \pm 58$  to  $106 \pm 71$  nm. The large standard error about the average is not caused by a lack of sampling size statistics but rather a result of the large distribution of grain sizes within the microstructure, as noted in the cumulative area fraction plot in Fig. 6c. Table 2 is a tabulation of the total number of grains counted in our PED analysis, which was more than one thousand and in some cases exceeded three thousand. A random reduction of the number of sampled grains by 25% and 50% did not change the average value or standard error. Only at a reduction of 75% of the grains counted was a modest shift in the average size noted, with this plot provided in the "Appendix". By providing the standard deviation to our average value in the text, we intend to capture the intrinsic large grain size distribution present in these types of samples while still providing a

**Table 2** The number of counted PED grains for each process and process condition

| Sample condition  | Total number of grains |
|-------------------|------------------------|
| Powder As-milled  | 1985                   |
| Powder annealed   | 1386                   |
| Film As-deposited | 3210                   |
| Film annealed     | 3090                   |

convenient means to track and discuss grain size changes based upon a single value, that being the average grain size. Although the average grain size increased following heating, the average grain size remains relatively low and appears at least partially stabilized. This confirms the prior stabilization reports, with no substantial grain growth in this material held at  $0.46 T_M$  of Cu for 24 h and then quenched from  $0.83 T_M$ .

### Thin films

The BF and HAADF images of the as-deposited and annealed Cu-3Zr (at%) film are shown in Fig. 7. Unlike the ball-milled sample, where the grains were acicular, here the grains are largely equiaxed (from the columnar vertical growth) in the plan-view direction which is typical for sputter deposition [53]. In the HAADF image, we note the presence of bright contrast regions along the grain boundaries and a few, isolated dark contrast features that are largely located at the triple junctions of the grains in the as-deposited film. The brighter contrast corresponds to a higher atomic number, i.e., Zr (rather than Cu), while the darker contrast could be associated with either an oxide, carbide, or oxy-carbide phase. Upon annealing, the overall distinctive bright (white) linear contrast in the boundaries appears to be reduced to a lower gray contrast, and the clear appearance of darker contrast features in some of the boundaries is more apparent. Furthermore, the darker features are no longer circular, Fig. 7b, but now appear to lie along the grain boundaries, Fig. 7d. To confirm the composition of these HAADF contrast phases, an XEDS spectral map was acquired, as shown in Fig. 8.

In Fig. 8a, the spatial compositional partitioning for the as-deposited film is not as distinct as compared to the annealed film, Fig. 8b. Nevertheless, one can detect thin regions of Zr decorating the grain boundaries, with a few such regions indicated by the white arrows in Fig. 8a to guide the reader. This

**Figure 7** **a** BF and **b** HAADF image of the as-deposited Cu–3Zr sample. **c** BF and **d** HAADF images of the heat-treated Cu–3Zr sample.

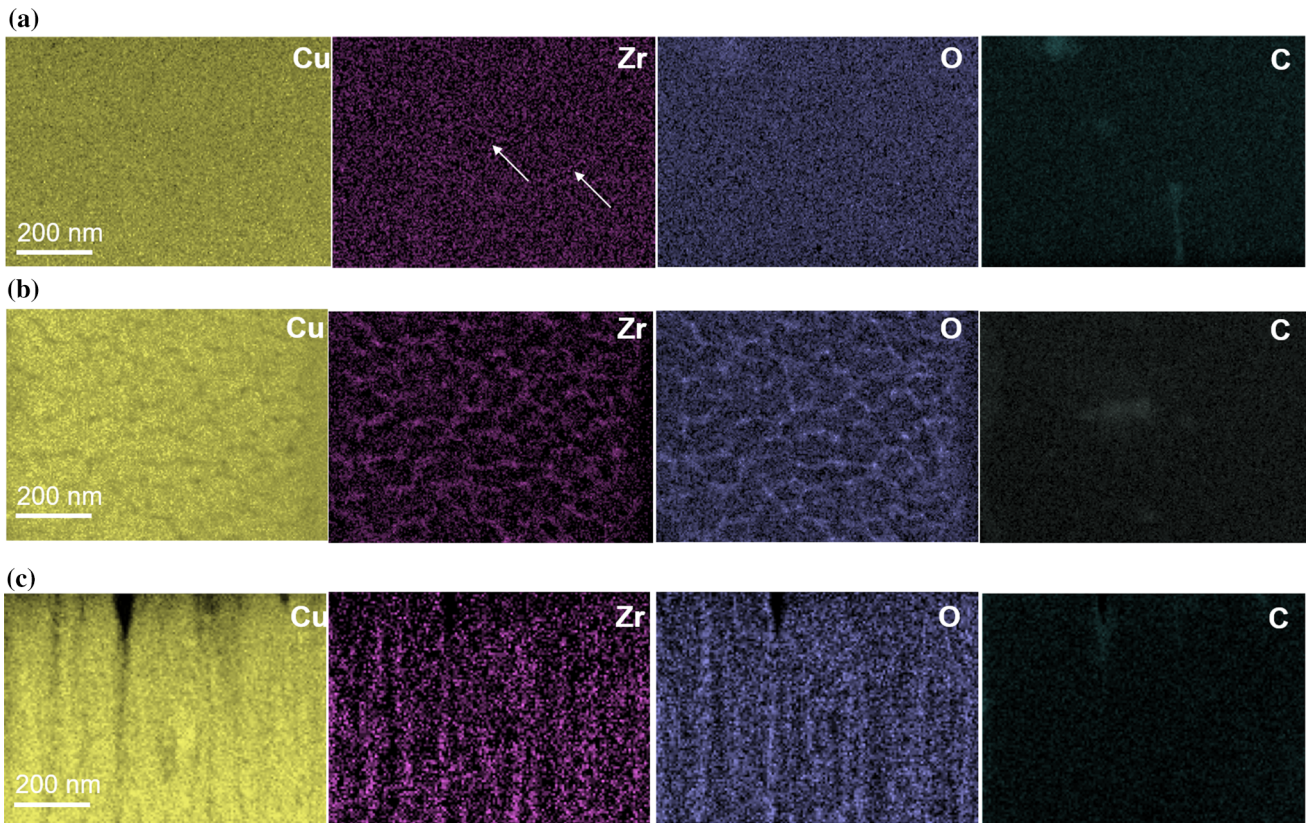
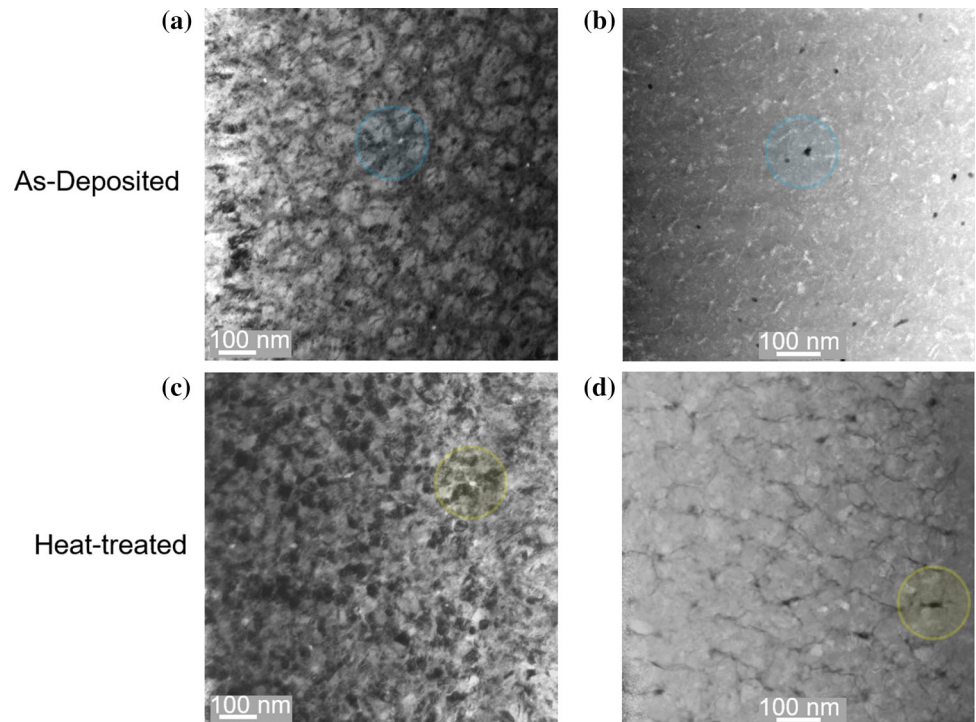


**Figure 8** XEDS elemental Cu, Zr, O, C maps of the **a** plan-view as-deposited and **b** plan-view heat-treated and **c** cross-sectional heat-treated Cu–3Zr samples.

suggests that the brighter contrast observed in the same regions in the STEM-HAADF image, Fig. 7b, is indeed Zr. Similarly, there are corresponding dark regions in the STEM-HAADF image, Fig. 7d, after annealing. At these boundaries, we have also detected O co-partitioning, Fig. 8(b), suggestive that the Zr in the boundaries is now oxidized. However, C partitioning to the grain boundaries is much less obvious, Fig. 8. This would propose that the darker contrast regions observed in the HAADF images, Fig. 7, are likely oxides. A cross-sectional TEM of the heat-treated thin film is shown in Fig. 8c. The Zr and O chemical partitioning is clearly evident with their chemical signals tracing along the columnar grain boundaries.

Table 1 displays the composition of the film in the as-deposited and annealed conditions, as determined by APT. In the as-deposited state, the thin film has a lower contaminant level than the as-processed ball-milled sample. There is a slight amount of O detected in the as-deposited film, which is thought to be as a result of intake from the background vacuum environment during deposition. No C or C-complexes were detected. The mass spectrum, Fig. 9, reveals a significant increase in the detection of oxide phase complexes upon annealing, with Table 1 revealing these measured amounts. In addition to  $\text{ZrO}^{+2}$ ,  $\text{ZrO}^{+1}$ , and  $\text{ZrO}_2^{+1}$  complexes,  $\text{ZrC}_2^{+1}$  was also captured. This increase in O capture is believed to be related to both the increase in Zr content in the film, as compared to the ball-milled sample studied, which innately getters more O, as well as the film's particular structure. The thin film has a substantially higher

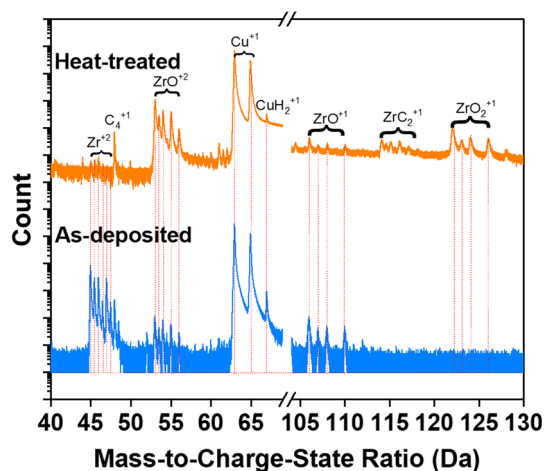


**Figure 9** Atom probe mass spectra of the as-deposited and heat-treated Cu–3Zr samples.

surface area-to-volume ratio as compared to a ball-milled powder. It is also worthy to note that the ball-milled APT specimen was retrieved from within the interior of the powder after being metallographically cross sectioned by polishing; in contrast, the entire thin film structure of the sputtered sample was extracted and prepared as the APT tip. Additionally, the film has long, linear columnar grain boundaries from the surface into the film's interior providing a 'fast-track' diffusion path. Even though the thin film provided an initially 'cleaner' system (less contaminants), these results suggest that this type of sample (geometry) can still be susceptible to other contaminant artifacts upon subsequent testing.

The atom map of the as-deposited film is shown in Fig. 10a. The 9% Zr(H) isoconcentration surface, near the top of the Cu atom map is contributed to being modest Zr partitioning to a grain boundary region. This partitioning can also be gleaned from the XEDS map of Fig. 8. A maximum separation method (MSM) was employed to identify if Zr clustering was present within the grains or other areas of the data set then those shown by the isoconcentration surface. No difference between the experimental data and a randomized data set could be ascertained, Fig. 10a. This provides strong evidence that Zr solutes are homogeneously distributed within the grain. In the heat-treated sample, clear chemical partitioning (clustering) is readily observed and is shown by the 25 at%  $\text{ZrO}_{1,2}$  and 2 at%  $\text{ZrC}_{1,2}$  isoconcentration surfaces (Fig. 10b). These particles were mainly composed of Zr–O complexes with some free O ions also detected. The overall ratio of O to Zr in this proxigram approaches  $\sim 2$ , indicating the formation of the  $\text{ZrO}_2$  phase.

The PED scans of the as-deposited and annealed thin film microstructures are shown in Fig. 11a. Besides the crystalline structure, regions with an amorphous structure (diffuse diffraction ring) were found and are represented as the white color in Fig. 11a. An example of the diffuse diffraction pattern is placed as an inset to these images and could be suggestive of being the previously reported AIFs. Such regions were not observed in the pre-annealed ball-milled powders examined by PED. This difference is likely associated with either the processing methods [33], the overall Zr solute content difference between the two samples studied (with the thin film having nearly  $3 \times$  more available Zr content for partitioning in the regions of interest characterized),

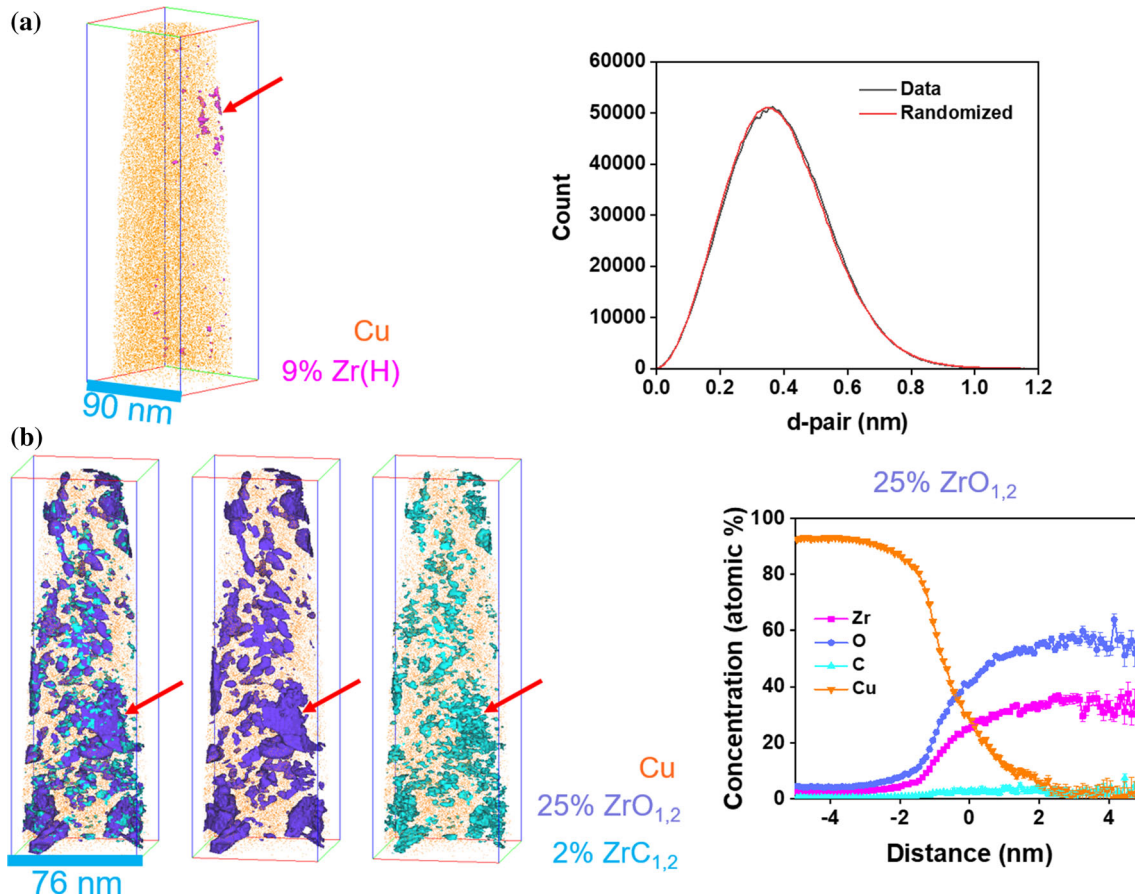


**Figure 10** **a** Atom probe map of the as-deposited Cu–3Zr sample and the corresponding Zr MSM cluster analysis result. **b** Atom probe maps of the heat-treated Cu–3Zr sample and the corresponding proxigram from the 25 at%  $\text{ZrO}_{1,2}$  isosurface.

and/or the relatively wider width of the AIF in the film enabling it to be more readily detected by PED. These AIFs in the thin film was  $\sim 15\%$  of the phase fraction of the deposited film's microstructure. The corresponding phase map reveals that the as-deposited thin film sample appears to have some sparse contaminant phases, i.e., one  $\text{ZrO}_2$  phase, which is highlighted by the black arrow in Fig. 11a. This phase would correspond to the small, dark contrast regions observed in the HAADF image in Fig. 7b. Finally, the pole figures from the PED scan, shown at the bottom of the PED dataset, reveals a strong  $\{111\}$  texture, which would be expected for an FCC deposited film in that it is the lowest surface energy [54]. In the grain mapping of the texture, this  $\{111\}$  orientation is blue, but many of these grains also contain a purplish color, which is near  $\langle 112 \rangle$  in the inverse pole figure. This orientation is attributed to the elastic strain effect created by the solubility of Zr within the matrix phase. Finally, a series of small  $\{110\}$  textured grains (green) appear to decorate some of the grains, with

several of these textures observed qualitatively near the amorphous regions.

Upon annealing the film, the thicker amorphous regions are no longer present. Thus, we can conclude that annealing leads to devitrification. The corresponding phase map by PED reveals  $\sim 1.2\%$   $\text{ZrO}_2$  (ICSD 56696) and  $\sim 0.6\%$   $\text{ZrC}$  phase (ICSD 22264) in the annealed film. Overall, the fraction of non-Cu phases, which includes Zr,  $\text{ZrO}_2$ , and  $\text{ZrC}$ , increased from  $\sim 0.1$  to  $\sim 2.2\%$  with post-processing heating. This correlates well with the increase in dark regions observed in the HAADF imaging after annealing (Fig. 7). The cumulative grain size histogram reveals a smaller grain size distribution than that of the ball-milled sample (Fig. 6c), evident by the increased gradient and smaller average grain sizes. Upon annealing, the average thin film grain size only slightly increased from  $40 \pm 28$  to  $45 \pm 29$  nm. Again, we note that the large standard deviation is intrinsic to the granular distribution by this process and not having sufficient grain counts, Table 2.

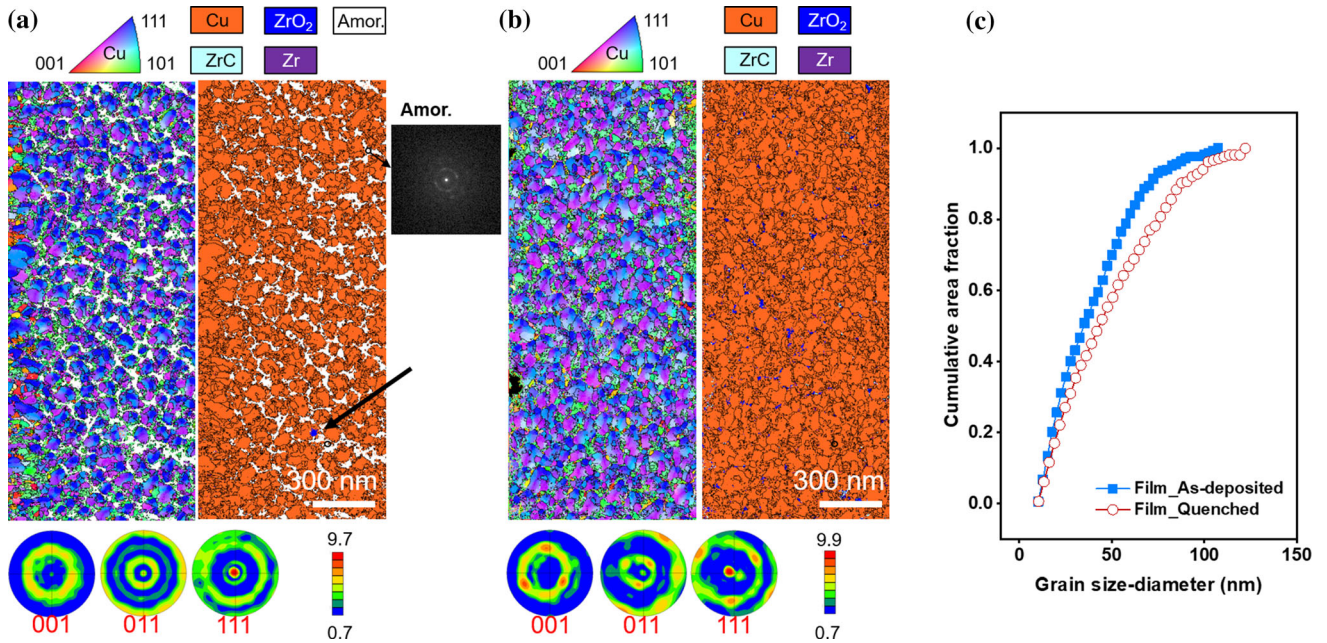


**Figure 11** PED orientation maps, phase map, pole figures, and selected diffraction pattern of the **a** as-deposited and **b** heat-treated Cu–3Zr samples. **c** cumulative grain size plots from (a) & (b).

A cross-correlative TEM and APT technique was employed to reveal the composition and chemical partitioning to specific grain boundaries in the annealed film. Figure 12a displays bright field images taken before and after field evaporation of the tip. The orientation map in Fig. 12b provides the crystalline information with the average grain size

being ~ 43 nm, which matches well with the larger PED scans shown above. Figure 12c shows the specific boundary types, which include low angle grain boundaries (LAGBs), high-angle grain boundaries (HAGBs), Σ3 boundaries, and twin boundaries. When comparing the grain boundary overlay with the XEDS map, Fig. 12d, the HAGBs appear to

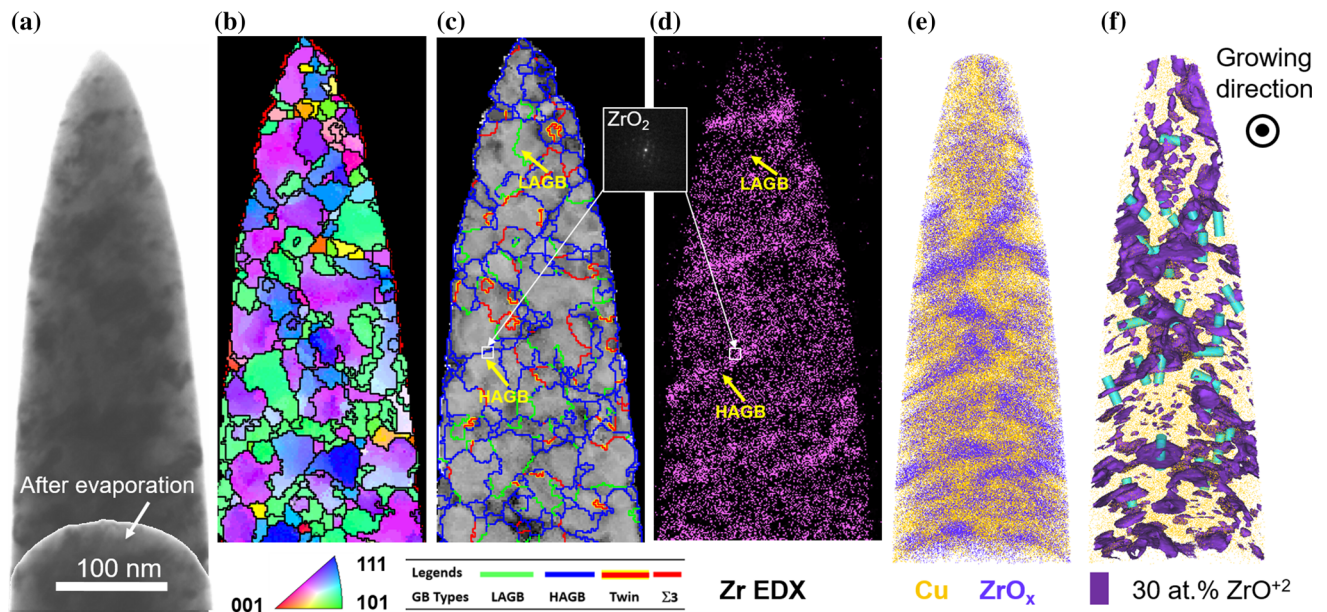


**Figure 12** **a** BF image **b** orientation map **c** grain boundary map **d** EDX elemental Zr map, and **e** atom map of the tip from the heat-treated Cu-3Zr film. **f** Atom map of the tip from the heat-treated

Cu–3Zr film with 30 at% ZrO<sup>+2</sup> isosurface embedded. 28 cylinders (light blue features) were also embedded in the dataset to calculate grain boundary interfacial excess.

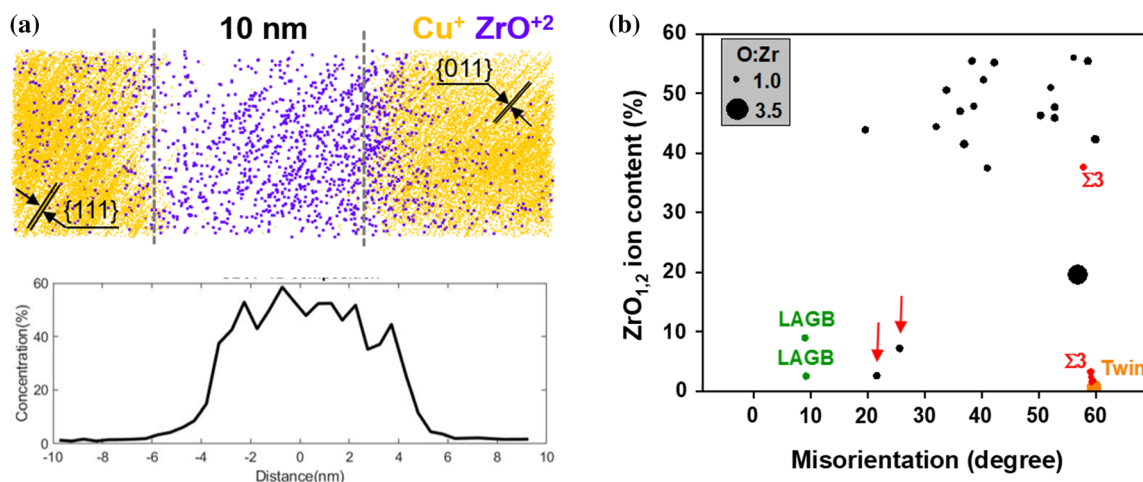
contain more Zr than the LAGBs. These HAGBs also correlate with the presence of  $ZrO_x$  in the atom map, Fig. 12e.

Figure 12(f) is an APT reconstruction of Fig. 12(e) with a 30 at. %  $ZrO^{+2}$  isosurface, which delineates the Zr lining the grain boundaries and in addition to showing Zr-rich small clusters or particles within such boundaries. The blue cylinders in Fig. 12f reveal the location of the various compositional profiles taken at the different grain boundaries. Figure 13a is a compositional profile across one of these representative HAGBs. Both ends of the cylinder are on either side of the grain, evident by the left Cu grain having an atomic {111} planar spacing and the grain on the left side having a {011} planar spacing. The center portion of the cylinder is the boundary region and is  $\sim 10$  nm in width. The collective width for all of the grain boundaries in Fig. 12 ranged from approximately 5–15 nm and match well with the reported HRTEM observation in Schuler et al.'s report for this alloy [32]. Figure 13b is a plot of the zirconium oxide content as a function of the misorientation angle taken from these cross-correlative images. Here, the oxide phase is linked to the boundary type where it is located. The smaller spheres denote an O/Zr ratio of approximately 1 whereas the larger sphere is 3.5. The LAGBs, the twin, and one of the  $\Sigma 3$  boundaries all revealed an approximate O/Zr ratio of 1. A similar O/Zr ratio can also be seen in the vast majority of the HAGBs. Note that all the data plotted was from a single data set that was field evaporated under the same

experimental conditions, ensuring that boundary type was the variable changed. This is important because the charge states are dependent on both the material properties as well as the experimental conditions for field evaporation. What is readily apparent in Fig. 13b is a higher content of the zirconium oxide is present in the HAGBs as compared to either LAGBs, the twin, and one of the  $\Sigma 3$  boundaries.

## Discussion

Regardless of the processing method, clear Zr chemical partitioning to the boundaries occurs in the powder and thin film samples in both the as-processed and heat-treated conditions for Cu–Zr. Nonetheless, the extent of Zr partitioning, reaction with contaminants, and its morphology in the microstructure varied between the processing routes. In the powder, most of the segregated Zr appeared as spherical or oval clusters, Figs. 1 and 2, from the onset of processing. These features remained relatively invariant upon annealing. In contrast, the sputter deposited film exhibited a more uniform distribution of Zr throughout the film, Figs. 8 and 9, with clear segregation to grain boundaries and dramatic increases in second phase reaction products upon annealing. This difference in Zr partitioning morphology is attributed to how the solute is imparted into the microstructure. Ball milling requires mechanical deformation mixing of the



**Figure 13** a Atom map and compositional profile across a representative HAGB the tip from the heat-treated Cu–3Zr. b  $ZrO_{1,2}$  content varies with misorientation angle. Symbol size

is proportional to O to Zr atomic ratio, which ranges from 1 to 3.5. LAGB was colored with green.  $\Sigma 3$  boundaries with red, and twin boundaries with orange. The rest black points are HAGBs.

powders, which is dependent upon the contact of the milling balls with the simultaneous impact of the Cu and Zr. This can yield a more localized means of mixing, where the imparted maximum stress breaks apart and mixes the Zr into the Cu. The deformation can lead to anisotropic granular morphologies, as seen in Fig. 6, and compositional variations within and between powders. In contrast, sputtering involves the ejection of each elemental species from a target and their collective condensation from the vapor over a uniform substrate. With the condensation onto the substrate, species nucleate, adopting initially hemispherical shaped caps leading to tighter and smaller grain sizes than the attrition powders, i.e., compare Figs. 6 and 11. Even though the sputtered Cu and Zr are condensed simultaneously, the low solubility of Zr in Cu was sufficient to drive a fraction of the Zr into the boundaries. This was seen in both the HAADF image, Fig. 7's brighter contrast at the boundaries, and the APT results shown in Fig. 10. With the more uniform distribution of Zr over the substrate, coupled with its preference to partition, its segregation was qualitatively found to be more uniform. Interestingly, these Zr-enriched regions clearly facilitated vitrification, evident by the significant fraction of amorphous grain boundaries in the as-deposited film (Fig. 11a). This could be expected since higher Zr compositions in Cu-Zr leads to the amorphization of thin films [55]. Here, the boundaries are biased to Zr enrichment by their tendency to phase separate. And, as mentioned previously, Schuler et al. [32] have reported the vitrification of such grain boundaries during Zr partitioning. Upon annealing the film, the Zr segregation in these boundary regions remained relatively unchanged; however, the presence of vitrified regions in the boundaries was no longer evident, Fig. 11b. Heating crystallizes these amorphous granular regions and also facilitates the Zr in this boundary region to readily react with the environment to form oxide scales in the boundaries, even though the film was annealed under vacuum. It should be noted that these amorphous regions observed prior to annealing are likely not the aforementioned AIFs, with such AIFs being reported to be less than 5 nm in width which is below the spatial resolution of the PED scan.

APT was employed as an ideal characterization method for identifying and quantifying impurities segregated to these grain boundaries in both processes. In addition to Zr, O was found to decorate

grain boundaries after annealing in both materials. This is attributed to Zr's high affinity for O, with grain boundaries likely to oxidize during the high-temperature heating process. Even in the as-processed specimens, low levels of O containing molecular ions were detected in the APT mass spectra, Figs. 3 and 9. However, prior to annealing, the overall amount of O detected was quite low for both material types, < 1 at% (Table 1). The carbon content was similarly low. This indicates that both processing routes are not subject to endemic quantities of contamination, but that what is present will react with the solute. Following annealing, the sputtered film appears to be much more susceptible to oxidation, in contrast to the ball-milled specimen. This difference likely results from the presence of Zr in its elemental state in the boundaries where it can readily react with the environment upon post-processing heating, whereas Zr in the as-milled powder has already undergone reaction with the contaminants.

This notable difference in the oxide content between the two processed samples is attributed to the initial Zr solute content and the specimen geometry. In the powder, a higher fraction of the oxide (and other non-Cu) phases was found. This was credited to both its inhomogeneity in mixing throughout the microstructure and Zr's reaction with the steric acid and other residual contaminants. The presence of a significant fraction of dark contrast features (oxides) in the HAADF, Fig. 1, coupled with a higher fraction of Zr-oxide complexes than elemental Zr in the APT runs in the as-milled condition, strongly suggests that any Zr in the powder will react with O and C before it is even annealed. Since the APT specimens for both as-milled and annealed states are taken from regions well within the interior portion of the powder, i.e., tens of microns from the surface after being metallographically polished in cross section, it is unlikely that additional oxidation of any elemental Zr occurred with post-annealing. Thus, for the powder samples, the intrinsic contamination reactions occur during fabrication. The various reacted products present at Zr-rich clusters further supports this conclusion. In Figs. 4 and 5, particular Zr particles revealed the presence of both O and C. Even though the total O content was low (~ 0.8%), coupled with a low Zr solute content (~ 1%) (Table 1), most of the solute was co-located with the available contaminant species present in the microstructure. This has been previously noted by

Kapoor et al. [28], where elemental solute only contributed to thermodynamic stabilization once it exceeded the contamination levels in the alloy.

In contrast, the film, which had a lower initial O level ( $\sim 0.2\%$ ) and a much higher Zr solute amount ( $\sim 3\%$ ) than the powder ( $\sim 1\%$ ), suffered from a significant increase in O concentration after annealing ( $\sim 5\%$ ). This uptake of O is believed to be associated with both the high presence of partitioned elemental Zr coupled with a large surface area-to-volume specimen geometry enabled the O to readily penetrate the sample. The residual O present during the vacuum anneal was able to diffuse quickly through the  $\sim 2\ \mu\text{m}$  thick film, particularly along the columnar grain boundaries where the elemental Zr was already present and ready to be oxidized. Furthermore, the HAADF image, Fig. 7d, and spectral XEDS mapping (Fig. 8) further supports the oxidation through the grain boundaries in the post-anneal condition. Hence, even if a ‘cleaner’ sample can be produced with a solute content that exceeds the initial processing contamination, how it then reacts with the environment may offset the processing gains, particularly when the solute has a high affinity for contaminate reactions. Even when great caution is taken in sample preparation, forethought must be given not only in controlling the initial processing contaminants, but the sample’s geometry and the post-processing treatments when studying stabilization mechanisms.

Figure 13b also provides additional insight into how these contaminates, in particular oxidation, varies between the boundary types. What is readily apparent from this figure is that HAGBs have a higher content of the zirconium oxide than the LAGBs, the twin, and one of the two  $\Sigma 3$  boundaries. In a recent report by Zhou and Thompson, HAGBs were noted to dominate the oxidation in nanocrystalline Fe(Cr) [56], with these results here in agreement with that study. The presence of a higher oxide content in the HAGBs is likely a result that these boundaries nominally have a higher solute content as compared to other special character boundaries [43]. The higher availability of the solute then enables a higher probability for oxidation. The difference in the oxide content between the two  $\Sigma 3$  boundaries is also contributed to this variability; Zhou et al. [43] noted a solute dependency in  $\Sigma 3$  as a function of boundary inclination. Collectively, these results reveal the dependency of the contamination (that is linked to

solute segregation) to the boundary characters in this nanocrystalline alloy.

Characterizing the presence and location of the solute and its reacted products now allows us to address their influence on nanocrystalline stability. It is clear that Zr partitioning to grain boundaries contributes to the stabilization of this alloy, but the specific stabilization mechanism is convoluted by its contaminant reactions. In prior work, the presence of AIFs in the grain boundaries, which were confirmed by HRTEM, were proposed as a stabilization mechanism [32]. Although vitrified boundaries were found in this study, they were thicker than the previously reported AIFs and also absent upon annealing. Even though such AIF structures have previously been found to exist in the same type of material processed as in this study, the lack of an abundantly observed AIF structure throughout the nanostructure boundary network suggests that other mechanisms are potentially contributing to the stability. In particular, the higher spatial and chemical sensitivity of atom probe, which allows for the detection of precipitates and clusters, may provide further information in quantifying these mechanisms.

In all cases, the smallest grain sizes were noted when secondary (contaminant) particles were present and readily observed throughout the boundary structure. For example, in the thin film case, where the grain size increased from an average of  $\sim 40\ \text{nm}$  to  $\sim 45\ \text{nm}$ , a significant fraction of all the boundaries contained these reacted product phases in the post-annealed state, with these phases making up  $\sim 2.2\ \text{vol}\%$  as measured by PED. In an attempt to quantify the grain boundary stabilization effect due to the presence of contaminant-rich particles (found by APT) that decorated the grain boundaries, we consider the classical Zener pinning prediction for grain size,  $d$  [23]. This is given as

$$d = \frac{0.4r}{f} \quad (1)$$

where  $f$  is the volume fraction of pinning particles, and  $r$  is the average pinning particle size. In our case, the PED measured volume fractions,  $f$ , is  $0.1\%$  (as-deposited) and  $2.2\%$  (annealed), with an average pinning particle radii of  $2.4\ \text{nm}$  and  $3.6\ \text{nm}$  respectively (Fig. 11). The Zener predicted grain size for the thin films are  $\sim 956\ \text{nm}$  and  $\sim 65\ \text{nm}$ , respectively. The larger predicted grain size for the non-annealed film values is not surprising since the fraction of

pinning particles is nearly non-existent. However, it does clearly reveal how the oxidation of Zr into a larger fraction of particles profoundly contributes to the stabilization. Upon annealing, and an increased fraction of pinning features, the predicted grain size is  $\sim 65$  nm. This size is nearly 40% larger than the measured grain sizes ( $\sim 45$  nm) for this sample. The lower experimental grain size could be caused by an excess of Zr at the grain boundaries, as observed via APT (Fig. 9) providing a thermodynamic contribution to stability. However, the significant reduction of detected elemental Zr upon annealing and the presence of O- and C-rich Zr clusters likely makes it a secondary effect. Closer inspection of the APT reconstruction of the annealed film in Fig. 12f reveals that the oxide isoconcentration surfaces are not just isolated particles, but are also linear (scale-like) features that track along the boundary. In such a 'wetting-like' morphology, the oxide phase provides a formidable structure to inhibit grain growth besides the simple, isolated particle assumption used in Eq. (1). APT's ability to provide this type of nanoscale representation of the oxide data is crucial in revealing how different stability mechanisms contribute to this alloy's nanocrystalline stability.

Using the same Zener estimation approach, the ball-milled sample's nanocrystalline stability can also be analyzed. Though both samples were initially prepared to have the same targeted Zr content, the lack of micro-homogeneity in the milled samples resulted microstructures that were characterized to have less Zr than the film. Thus, any direct comparisons between the two processes in terms of stability should be made with caution; nevertheless, the differences in Zr content provides an opportunity to infer the relative importance of Zr content on general stability. Furthermore, the difference in content also does not change the results, discussion or forthcoming conclusions concerning how contamination may impact stability for a particular process of fabrication. Based on the PED data, the as-milled powder's average grain size was  $\sim 76$  nm, with the non-Cu secondary phase fraction being  $\sim 2.6\%$  and the pinning particle sizes being  $\sim 12$  nm. Using these input parameters, the predicted Zener pinned grain size would be  $\sim 184$  nm, with the PED observed size being  $\sim 106$  nm. However, the PED scan of the annealed powder grain size had an even smaller detected secondary phase fraction of  $\sim 0.7$  vol% than the aforementioned as-milled sample. If we use

the experimental phase fraction from the PED dataset for the annealed powder grains, the Zener pinned grain size is predicted to be  $\sim 345$  nm. This highlights an important aspect in reporting nanocrystalline grain sizes. One should directly quantify the chemical and structural contaminant fraction from the exact sample itself so that self-contained comparisons are made. This would suggest that another mechanism for promoting the smaller grain size is present. The limited spatial resolution of PED is likely not capturing these contributing mechanism features.

APT is again able to provide potential insights that are not necessarily captured in the TEM analysis for such mechanisms. Figure 5 revealed that the annealed powder has the presence of many small O- and C-rich clusters within its grain boundaries. From this APT dataset, the volume fraction measured from these potential pinning features is  $\sim 4.7\%$ , with an average pinning particle size of  $\sim 3.8$  nm. These new values yield a predicted Zener pinned grain size of  $\sim 32$  nm, which is more than one hundredth the actual annealed grain size measured. A smaller Zener pinned grain size than measured is also calculated using the APT dataset of the as-milled powder in Fig. 4 (volume fraction  $\sim 3.5\%$  and particle size  $\sim 3.8\%$ ). With the experimentally measured grain sizes bounded by the lower APT input data and the upper PED predicted values, a definitive conclusion of the exact stability mechanism, AIFs (as previously reported) or contaminate clusters as shown here, is arguably still elusive. It is suspected that the inhomogeneity characterized within the powder itself contributes to this issue; this furthers complicates the identification of which competing mechanisms is responsible for the stability mechanism in this system.

In the initial milling of the powders, where the Cu nanocrystallites are formed through high-energy ball impacts, the Zr is not uniformly distributed in the mixture to control and narrow the grain size. This could be a result of the solute reacting with the intrinsic contaminants from the process itself, which was confirmed by both oxide and carbide particles being found in the as-milled condition. The presence of an oxide and/or carbide has an adverse influence on Zr's ability to (1) plastically deform, (2) be mechanically driven into solution to later precipitate out onto the boundaries [28], and (3) distribute itself uniformly along the grain boundaries. Thus, some

boundaries would have pinning particles while others would be absent. This is evident when considering the grain size variation in Fig. 6. The standard deviation about the average grain size is  $76 \pm 58$  nm (as-milled) and  $106 \pm 71$  nm (annealed). In contrast, the thin film had elemental Zr distributed across the boundaries upon deposition and, upon annealing, the solute then reacted with the environment to subsequently form either oxide particles or an oxide scale-like morphology within the boundaries. Consequently, the grain sizes remained relatively similar in both their average value and standard deviation about that average, i.e.,  $40 \pm 28$  nm (as-deposited) and  $45 \pm 29$  nm (annealed).

Though AIFs have been reported previously in this alloy [32], the prevalent reactions of Zr with O and C, Fig. 3, and the APT detection of small scale secondary phase clusters within the boundaries, Fig. 5, are more likely significant contributors to any coupled stability mechanism. Though prior reports have suggested a weighted reduction of grain boundary energy as the dominant mechanism for stabilization [30], the application of atom probe, with its unique characteristic of high chemical and spatial resolution, provides more clarity regarding the complex nature of ascertaining how solutes in grain boundaries provide stability. Indeed, the use of atom probe and the detection of nanoscale solute-rich O and C clusters/particles further outlined the importance of contamination with regards to grain boundary stabilization in nanocrystalline alloys.

## Conclusions

In this article, two forms of nanocrystalline stabilized Cu-Zr alloy fabrication were compared—ball milling and thin film deposition. The evolution of grain size, chemical partitioning, solute reactions with contaminants, and grain boundary specific segregation were characterized and addressed. From this analysis we aim to provide further clarity of how impurities and planned solutes interact to stabilize nanocrystalline microstructures. The following major conclusions are drawn:

- In the powder sample, Cu-1Zr, the as-milled and annealed samples had grain sizes of  $76 \pm 58$  and  $106 \pm 71$  nm, respectively. The thin film sample, Cu-3Zr, as-deposited and annealed

samples had grain sizes of  $40 \pm 28$  and  $45 \pm 29$  nm, respectively. The differences in grain sizes are largely attributed to the method of fabrication. In ball milling, the solute is mechanically mixed into the alloy while the powder particulates undergo deformation to form small crystallites. During this deformation micro-chemical inhomogeneity of the solute in the matrix appears to exist. In sputter-deposition, the elements undergo a more ‘homogeneous’ mixing as they condense onto the substrate from the vapor.

- APT revealed that both methods, in the as-prepared condition, were arguably clean with  $< 1\%$  O. However, in the powder state, nearly all of the Zr solute was found in O- and C-rich particles. Upon annealing, no significant change in reaction products was observed. In the thin film samples, the as-deposited film was largely absent from any oxide (or carbide) secondary phases, with clear evidence of elemental Zr partitioning in the boundaries. PED scans revealed many of these boundaries were vitrified with widths between  $\sim 5$ – $15$  nm. Upon annealing, these boundaries were no longer amorphous and the majority of the Zr reacted and formed oxides, both as small, separate particles as well as continuous features along the length of the boundaries. This uniform oxidation of the solute has been attributed to the high surface area-to-volume ratio of the film coupled with columnar grains enriched with elemental Zr, which facilitated an ultimately higher O uptake ( $\sim 5\%$ ) after annealing.
- For the powder samples, no amorphous regions in the boundaries, as characterized by PED, were observed in either the as-milled or annealed conditions. This may be a result of the limited spatial resolution of PED to prior reports to the thicknesses of thin AIFs. In the ball milling process, contamination, at least for this alloy and its preparation, is prevalent upon initial fabrication. Consequently, the contaminate reaction with the solute in the as-processed condition contributed to inhomogeneity of the solute distribution within the grain boundaries ultimately influencing the pinning effects for stabilizing the nanocrystallites throughout the microstructure.
- Using a simple Zener predicted pinned grain size estimate, the effect of these secondary phases on stability was discussed. For the sputtered thin films, the measured grain sizes were found to be

lower than the Zener predicted sizes. Though other contributors to stability may explain this observation, the clear loss of elemental Zr to the oxide phase suggests that any thermodynamic effect is lessened. Rather, in some areas, the oxide phases that would follow and ‘wet’ the boundary providing a potent barrier for grain growth. For the powder samples, inhomogeneity distributions of the solute were clearly noted in the PED scans, which made Zener pinning contributions more difficult to ascertain. Nonetheless, APT revealed small secondary phase clusters in the grain boundaries that would assist in a Zener-like mechanism. The solute, already in a reacted state before annealing, also reduced the probability of an elemental solute thermodynamic mechanism in reducing the boundary energy. Prior work has shown AIFs in these boundaries, which were proposed as a stability mechanism. Though these structures were not detected by PED, likely because of spatial resolution limitation noted above, the use of APT does provide new and additional information. The prevalent oxidation of the solute, in the as-processed or post-annealed condition, and its similarly small-scale features in the boundaries would be a contributing mechanism to the nanocrystalline stability.

- As with all processing, variations in preparatory conditions can influence the extent of contamination. For ball milling this includes milling media, milling environment, use of milling agents like stearic acid and its concentration; for thin films it would be the purity of the sputtering target, background levels of contaminate gases (like oxygen or nitrogen), and the chamber itself. Nevertheless, this paper has highlighted, at least for Cu(Zr), their influence between each process and concerns one should be aware of as different stabilized alloys are investigated. Future work can more specifically address variations in preparatory conditions to better ascertain their influence within the process itself.
- When discussing or determining the nanoscale stability mechanism, it is essential that high-resolution analytical characterization of the material’s composition and structure be performed. In doing so, a complete representation of how the elements are distributed and react with potential contaminants is apparent, which can have a

dramatic influence on determining the mechanisms of stability.

## Acknowledgements

XZ and GBT gratefully acknowledge NSF-DMR-1709803 for support of this research, which involved the characterization and analysis of the APT datasets. JS, CG, and TJR acknowledge the U.S. Army Research Office under Grant W911NF-16-1-0369 for the specimens and technical discussion. LL recognizes US National Science Foundation under Grant CMMI 17-0267 for technical discussion in the implication of the findings on phase stability. The UA Central Analytical Facility is recognized for additional assistance and access to the microscopes used in this research.

## Appendix

The appendix section provides additional information concerning the sampling sizes for the grain size analysis of each of the samples. Referring to Table 2, the number of grains were randomly reduced to

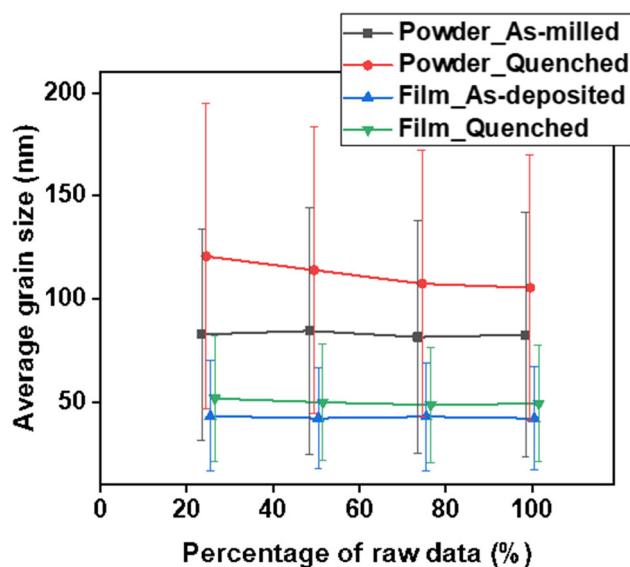


**Figure 14** Plot of average grain size and one standard deviation by the random reduction of grain sizes from the total number of grain counted given in Table 2. Note the relative invariance of the average and error, indicating that the grain size deviation about the average is intrinsic to the processed microstructure and not a result of low counting statistics.

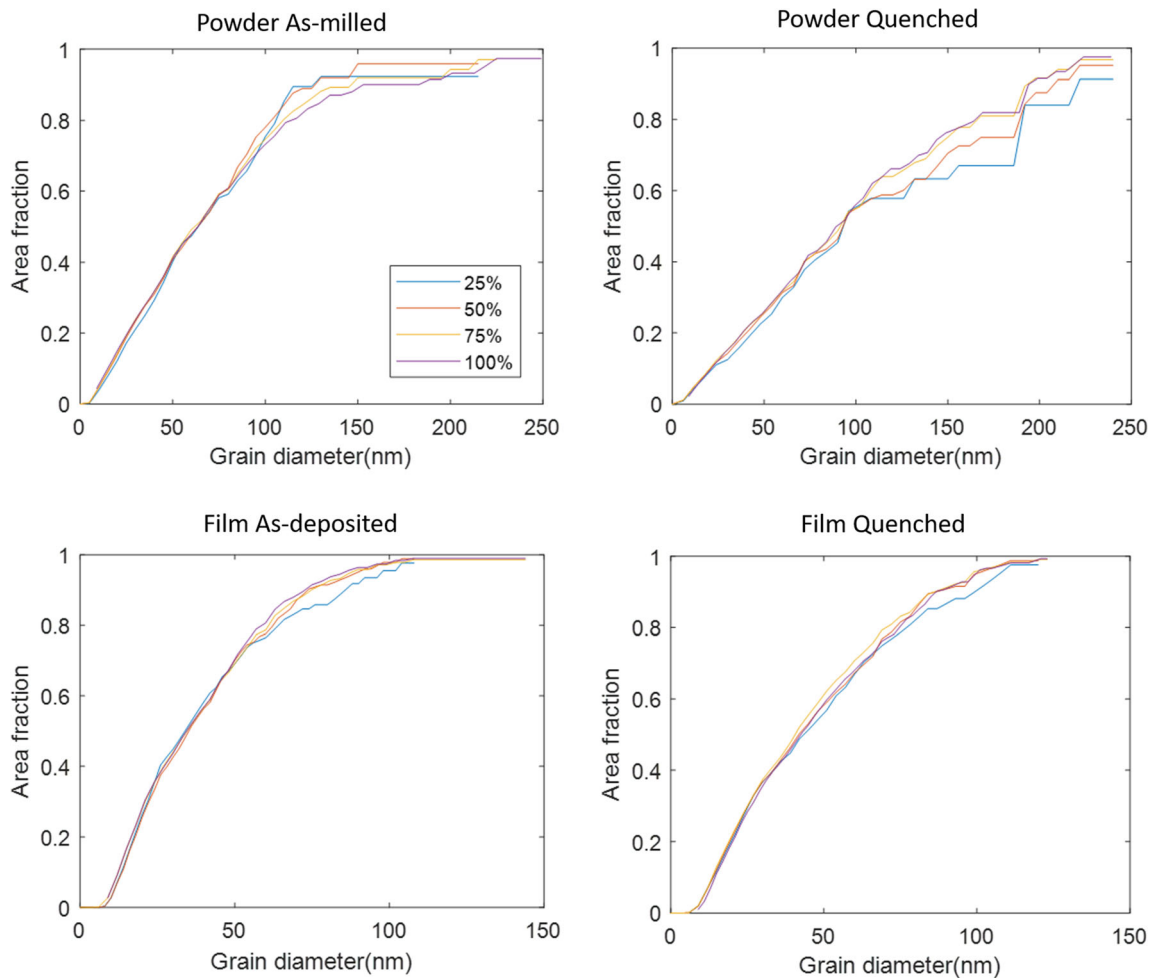


**Figure 15** Cumulative area fraction maps with a random reduction of the counted grain sizes given in Table 2. This absent or near modest changes with reduced number of counted

determine if the error and/or average value changed. This has been plotted for the average value, and its standard deviation, in Fig. 14, with the cumulative area fractions in Fig. 15.

## References

- [1] Zhu YT, Liao XZ, Wu XL (2012) Deformation twinning in nanocrystalline materials. *Prog Mater Sci* 57(1):1–62
- [2] Li HQ, Choo H, Ren Y, Saleh TA, Lienert U, Liaw PK, Ebrahimi F (2008) Strain-dependent deformation behavior in nanocrystalline metals. *Phys Rev Lett* 101(1):015502
- [3] Sanders PG, Eastman JA, Weertman JR (1997) Elastic and tensile behavior of nanocrystalline copper and palladium. *Acta Mater* 45(10):4019–4025
- [4] Lu L, Sui ML, Lu K (2000) Superplastic extensibility of nanocrystalline copper at room temperature. *Science* 287:1463–1466
- [5] Liddicoat PV, Liao XZ, Zhao Y, Zhu Y, Murashkin MY, Lavernia EJ, Valiev RZ, Ringer SP (2010) Nanostructural hierarchy increases the strength of aluminium alloys. *Nat Commun* 1:63
- [6] Rupert TJ, Schuh CA (2010) Sliding wear of nanocrystalline Ni–W: structural evolution and the apparent breakdown of Archard scaling. *Acta Mater* 58(12):4137–4148
- [7] Darling K, Rajagopalan M, Komarasamy M, Bhatia M, Hornbuckle B, Mishra R, Solanki K (2016) Extreme creep resistance in a microstructurally stable nanocrystalline alloy. *Nature* 537(7620):378–381
- [8] Gleiter H (1989) Nanocrystalline materials. *Prog Mater Sci* 33(4):223–315

- [9] Andrievski RA (2014) Review of thermal stability of nanomaterials. *J Mater Sci* 49(4):1449–1460. <https://doi.org/10.1007/s10853-013-7836-1>
- [10] Tschopp MA, Murdoch HA, Kecskes LJ, Darling KA (2014) “Bulk” nanocrystalline metals: review of the current state of the art and future opportunities for copper and copper alloys. *JOM* 66(6):1000–1019
- [11] Weissmüller J (1993) Alloy effects in nanostructures. *Nanostruct Mater* 3:261–272
- [12] Chookajorn T, Murdoch HA, Schuh CA (2012) Design of stable nanocrystalline alloys. *Science* 337(6097):951–954
- [13] Nes E, Ryum N, Hunderi O (1985) On the zener drag. *Acta Metall* 33(1):11–22
- [14] Krill CE, Ehrhardt H, Birringer R (2005) Thermodynamic stabilization of nanocrystallinity. *Z Metallkd* 96(10):1134–1141
- [15] Darling KA, VanLeeuwen BK, Koch CC, Scattergood RO (2010) Thermal stability of nanocrystalline Fe–Zr alloys. *Mater. Sci. Eng. A* 527(15):3572–3580
- [16] Darling KA, Kecskes LJ, Atwater M, Semones J, Scattergood RO, Koch CC (2013) Thermal stability of nanocrystalline nickel with yttrium additions. *J Mater Res* 28(13):1813–1819
- [17] Atwater MA, Roy D, Darling KA, Butler BG, Scattergood RO, Koch CC (2012) The thermal stability of nanocrystalline copper cryogenically milled with tungsten. *Mater. Sci. Eng. A* 558:226–233
- [18] Amram D, Schuh CA (2018) Interplay between thermodynamic and kinetic stabilization mechanisms in nanocrystalline Fe–Mg alloys. *Acta Mater* 144:447–458
- [19] Murdoch HA, Schuh CA (2013) Stability of binary nanocrystalline alloys against grain growth and phase separation. *Acta Mater* 61(6):2121–2132
- [20] Darling KA, Tschopp MA, VanLeeuwen BK, Atwater MA, Liu ZK (2014) Mitigating grain growth in binary nanocrystalline alloys through solute selection based on thermodynamic stability maps. *Comput Mater Sci* 84:255–266
- [21] Koju RK, Darling KA, Kecskes LJ, Mishin Y (2016) Zener pinning of grain boundaries and structural stability of immiscible alloys. *JOM* 68(6):1596–1604
- [22] Manohar PA, Ferry M, Chandra T (1998) Five decades of the zener equation. *ISIJ Int* 38(9):913–924
- [23] Doherty RD (2012) Grain coarsening—insights from curvature modeling cyril stanley smith lecture. *Mater Sci Forum* 715–716:1–12
- [24] Cantwell PR, Tang M, Dillon SJ, Luo J, Rohrer GS, Harmer MP (2014) Grain boundary complexions. *Acta Mater* 62:1–48
- [25] Dillon SJ, Tang M, Carter WC, Harmer MP (2007) Complexion: a new concept for kinetic engineering in materials science. *Acta Mater* 55(18):6208–6218
- [26] Koju RK, Darling KA, Solanki KN, Mishin Y (2018) Atomistic modeling of capillary-driven grain boundary motion in Cu–Ta alloys. *Acta Mater* 148:311–319
- [27] Rajagopalan M, Darling K, Turnage S, Koju RK, Hornbuckle B, Mishin Y, Solanki KN (2017) Microstructural evolution in a nanocrystalline Cu–Ta alloy: a combined in situ TEM and atomistic study. *Mater Des* 113:178–185
- [28] Kapoor M, Kaub T, Darling KA, Boyce BL, Thompson GB (2017) An atom probe study on Nb solute partitioning and nanocrystalline grain stabilization in mechanically alloyed Cu–Nb. *Acta Mater* 126:564–575
- [29] Atwater MA, Scattergood RO, Koch CC (2013) The stabilization of nanocrystalline copper by zirconium. *Mater. Sci. Eng. A* 559:250–256
- [30] Khalajhedayati A, Rupert TJ (2015) High-temperature stability and grain boundary complexion formation in a nanocrystalline Cu–Zr alloy. *JOM* 67(12):2788–2801
- [31] Khalajhedayati A, Pan ZL, Rupert TJ (2016) Manipulating the interfacial structure of nanomaterials to achieve a unique combination of strength and ductility. *Nat Commun* 7:10802
- [32] Schuler JD, Rupert TJ (2017) Materials selection rules for amorphous complexion formation in binary metallic alloys. *Acta Mater* 140:196–205
- [33] Zhao JT, Zhang JY, Cao LF, Wang YQ, Zhang P, Wu K, Liu G, Sun J (2017) Zr alloying effect on the microstructure evolution and plastic deformation of nanostructured Cu thin films. *Acta Mater* 132:550–564
- [34] Almyras GA, Matenoglou GM, Komninou P, Kosmidis C, Patsalas P, Evangelakis GA (2010) On the deposition mechanisms and the formation of glassy Cu–Zr thin films. *J Appl Phys* 107(8):084313
- [35] Marvel CJ, Yin D, Cantwell PR, Harmer MP (2016) The influence of oxygen contamination on the thermal stability and hardness of nanocrystalline Ni–W alloys. *Mater. Sci. Eng. A* 664:49–57
- [36] Marvel CJ, Cantwell PR, Harmer MP (2015) The critical influence of carbon on the thermal stability of nanocrystalline Ni–W alloys. *Scr Mater* 96:45–48
- [37] Baker FB, Storms EK, Holley CE (1969) Enthalpy of formation of zirconium carbide. *J Chem Eng Data* 14(2):244–246
- [38] Chase MW Jr (1998) NIST-JANAF thermochemical tables, 4th edn. American Chemical Society, Woodbury, NY
- [39] Kelly TF, Miller MK (2007) Atom probe tomography. *Rev Sci Instrum* 78(3):031101
- [40] Guo W, Jagle EA, Choi PP, Yao JH, Kostka A, Schneider JM, Raabe D (2014) Shear-induced mixing governs

- codeformation of crystalline-amorphous nanolaminates. *Phys Rev Lett* 113(3):035501
- [41] Guo W, Yao J, Jäggle EA, Choi P-P, Herbig M, Schneider JM, Raabe D (2015) Deformation induced alloying in crystalline—metallic glass nano-composites. *Mater Sci Eng A* 628:269–280
- [42] Guo W, Gan B, Molina-Aldareguia JM, Poplawsky JD, Raabe D (2016) Structure and dynamics of shear bands in amorphous-crystalline nanolaminates. *Scr Mater* 110:28–32
- [43] Zhou X, Yu X-X, Kaub T, Martens RL, Thompson GB (2016) Grain boundary specific segregation in nanocrystalline Fe(Cr). *Sci Rep* 6:34642
- [44] Moeck P, Rouvimov S, Rauch EF, Véron M, Kirmse H, Häusler I, Neumann W, Bultreys D, Maniette Y, Nicolopoulos S (2011) High spatial resolution semi-automatic crystallite orientation and phase mapping of nanocrystals in transmission electron microscopes. *Cryst Res Technol* 46(6):589–606
- [45] Rauch EF, Portillo J, Nicolopoulos S, Bultreys D, Rouvimov S, Moeck P (2010) Automated nanocrystal orientation and phase mapping in the transmission electron microscope on the basis of precession electron diffraction. *Z Kristallogr* 225(2–3):103–109
- [46] Brons J, Thompson G (2014) Orientation mapping via precession-enhanced electron diffraction and its applications in materials science. *JOM* 66(1):165–170
- [47] Thompson K, Lawrence D, Larson DJ, Olson JD, Kelly TF, Gorman B (2007) In situ site-specific specimen preparation for atom probe tomography. *Ultramicroscopy* 107(2–3):131–139
- [48] Hornbuckle B, Kapoor M, Thompson G (2015) A procedure to create isoconcentration surfaces in low-chemical-partitioning, high-solute alloys. *Ultramicroscopy* 159:346–353
- [49] Barton DJ, Hornbuckle BC, Darling KA, Thompson GB (2019) The influence of isoconcentration surface selection in quantitative outputs from proximity histograms. *Microsc Microanal* 25:401–409
- [50] Commercial product—Silicon half grids. <http://www.microscopyconsumables.com/product-p/grd-0002.04.10.htm>.
- [51] Zhou X, Thompson GB (2019) Charge-state field evaporation behavior in Cu(V) nanocrystalline alloys. *Microsc Microanal* 25:501–510
- [52] Grigorian CM, Rupert TJ (2019) Thick amorphous complexion formation and extreme thermal stability in ternary nanocrystalline Cu–Zr–Hf alloys. *Acta Mater* 179:172–182
- [53] Zhou X, Kaub T, Martens RL, Thompson GB (2016) Influence of Fe(Cr) miscibility on thin film grain size and stress. *Thin Solid Films* 612(1):29–35
- [54] Gungor A, Barmak K, Rollett AD, Cabral Jr C, Harper JME (2002) Texture and resistivity of dilute binary Cu(Al), Cu(In), Cu(Ti), Cu(Nb), Cu(Ir), and Cu(W) alloy thin films. *J Vac Sci Technol B* 20(6):2314–2319
- [55] Sterwerf C, Kaub T, Deng C, Thompson GB, Li L (2017) Deformation mode transitions in amorphous-Cu<sub>45</sub>Zr<sub>55</sub>/crystalline-Cu multilayers. *Thin Solid Films* 626:184–189
- [56] Zhou X, Thompson GB (2019) In situ TEM observations of initial oxidation behavior in Fe-rich Fe–Cr alloys. *Surf Coat Technol* 357:332–338

**Publisher's Note** Springer Nature remains neutral with regard to jurisdictional claims in published maps and institutional affiliations.